


Vector Magnetometry Exploiting Phase-Geometry Effects in a Double-Resonance Alignment Magnetometer

Stuart J. Ingleby,^{*} Carolyn O'Dwyer, Paul F. Griffin, Aidan S. Arnold, and Erling Riis
Department of Physics, SUPA, Strathclyde University, 107 Rottenrow East, Glasgow, UK

 (Received 2 March 2018; revised manuscript received 15 June 2018; published 18 September 2018)

Double-resonance optically pumped magnetometers are an attractive instrument for unshielded magnetic-field measurements due to their wide dynamic range and high sensitivity. The use of linearly polarized pump light creates alignment in the atomic sample, which evolves in the local static magnetic field, and is driven by a resonant applied field perturbation, modulating the polarization of transmitted light. We demonstrate experimentally that the amplitude and phase of observed first- and second-harmonic components in the transmitted polarization signal contain sufficient information to measure the static-magnetic-field magnitude and orientation. We describe a laboratory system for experimental measurements of these effects and verify a theoretical derivation of the observed signal. We demonstrate vector-field tracking under varying static-field orientations and show that the static-field magnitude and orientation may be observed simultaneously, with an experimentally realized resolution of 1.7 pT and 0.63 mrad in the most sensitive field orientation.

DOI: [10.1103/PhysRevApplied.10.034035](https://doi.org/10.1103/PhysRevApplied.10.034035)

I. INTRODUCTION

Unshielded magnetic-field measurements are a key technique in applications ranging from mineral surveying [1] to archaeology [2] and the development of compact femtotesla-sensitivity magnetometers [3] may lead to significant advances in these applications. The measurement of the gradients and curvature in an arbitrarily oriented static magnetic field are of critical importance. The practical difficulties associated with developing portable cryogenic systems for superconducting-quantum-interference-device (SQUID)-based magnetometers make the development of optically pumped atomic magnetometers attractive. Unshielded optically pumped gradiometers have been demonstrated recently [4], using a double-resonance magnetometry scheme. In this work, we demonstrate a double-resonance magnetometer in which measurement of the full magnetic-field vector is achieved through the observation of geometry-dependent phase variations in the first- and second-harmonic components of the measured atomic response to a resonant alternating field modulation.

In double-resonance magnetometers, such as this one, the evolution of atomic spins in a static field \vec{B}_0 is driven by modulation at a frequency ω_{rf} , with a resonant response when ω_{rf} is equal to a harmonic of the atomic Larmor frequency $\omega_L = \gamma|B_0|$. γ is the gyromagnetic ratio for the probed atomic ground state. The modulation may

take the form of oscillating-pump light amplitude [5], polarization [6], or frequency [7] or (this work) a small oscillating applied field \vec{B}_{rf} [8]. For alkali-metal vapor magnetometers operating in the geophysical field range $\omega_{\text{rf}} \approx \mathcal{O}(2\pi \times 100 \text{ kHz})$, a convenient frequency range for digitization and software signal analysis, making double-resonance magnetometry a useful technique for uncompensated portable unshielded magnetometry, combining a high dynamic range and high sensitivity. In order to develop techniques for compact sensors with low cost and power consumption, we use a single monochromatic pump-probe laser beam and apply a small magnetic-field perturbation to resonantly drive atomic-spin precession. The precessing atomic spins modulate the Faraday rotation of the atomic cell and are detected by measurement of the polarization of transmitted light.

Double-resonance sensors have been used widely in scalar-field measurements for many years [9–11]. Locking ω_{rf} to ω_L using the dispersive component of the demodulated signal response allows $|B_0|$ to be determined readily. However, this technique requires that the demodulation phase be set *a priori* and only yields information on the magnitude of \vec{B}_0 . In addition, the signal amplitude in double-resonance magnetometry is highly dependent on the orientation of \vec{B}_0 relative to \vec{B}_{rf} and the axis of light propagation. Orientations of \vec{B}_0 with zero signal amplitude are known as *dead zones*. We note that measurement schemes for dead-zone reduction or dead-zone-free magnetometry have been demonstrated successfully [12]. In this paper, we demonstrate a sensor configuration and

^{*}stuart.ingleby@strath.ac.uk

analysis scheme for determination of the \vec{B}_0 orientation from the measured phases of the signal contributions observed at ω_{rf} and $2\omega_{\text{rf}}$. We show that the detected signal can be analyzed using an atomic-alignment model to determine the magnitude and orientation of \vec{B}_0 , allowing the full field vector to be inferred.

Various other schemes for vector-atomic magnetometry have been demonstrated, including zero-field sensors [13,14], orthogonal probe lasers [15,16], orthogonal pump lasers [17], measurement of EIT (electromagnetically induced transparency) resonances [18], and application of significant quasistatic \vec{B}_0 perturbations [19–21]. The scheme demonstrated here complements these approaches by addressing some of their practical drawbacks. Zero-field techniques are well suited for shielded measurements, but lack the dynamic range required for portable unshielded measurements, and additionally require full-field compensation. The use of compensation coils, additional light frequencies or beams, and additional \vec{B}_0 perturbations add significant hardware overheads and power requirements. We also wish to avoid vector-magnetometry schemes requiring sequential measurements under varying field conditions, or observation of free-induction decay signals, as these methods require longer sampling times and may ultimately limit the achievable sensor bandwidth.

II. THEORY

A simple single-beam M_x magnetometer configuration is used, but the geometry of the static and modulating magnetic fields, the atomic sample, and the analysis optics is critical to the analysis technique and is shown in detail in Fig. 1. A half-wave plate is used to balance the detector by rotating the linear polarization of transmitted light by 45° , meaning that light that is x polarized prior to the atoms is equally split by the analyzer. The observed differential signal is equal to the difference in transmission of the two orthogonal components separated by the polarizing beam splitter. With this configuration, the observed signal is modulated due to the precession of atomic-alignment moments (see Ref. [22]) under the magnetic fields \vec{B}_0 and \vec{B}_{rf} .

The absorption of linear polarization states by the atomic sample varies with the evolution of the polarization alignment moments in the sample. If the light-polarization axis defines the quantization axis, then the light-absorption coefficient is proportional to

$$\kappa \propto \frac{A_0}{\sqrt{3}} m_{0,0} - \sqrt{\frac{2}{3}} A_2 m_{2,0}, \quad (1)$$

where the analysing powers A_0 and A_2 depend on the hyperfine states coupled by the light, and the multipole

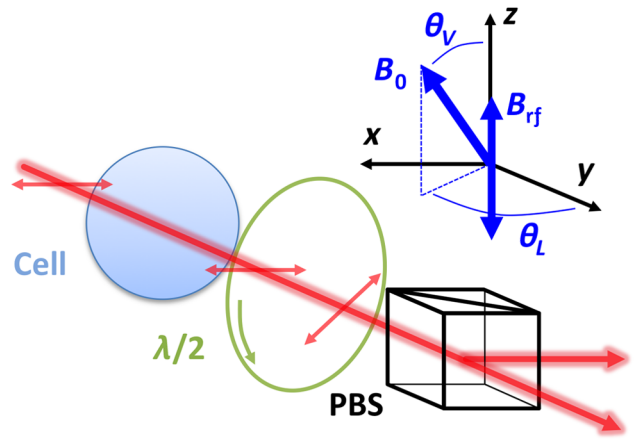


FIG. 1. An isometric-projection schematic showing the reference frame used. The orientation of the static magnetic field \vec{B}_0 is described by the spherical polar angles θ_V and θ_L , and the oscillating magnetic field applied on the z axis. The intensity difference between orthogonal components of light transmitted through the cell is measured using a differential photodetector (not shown).

moments $m_{k,q}$ describe the polarization of the atomic sample [23].

We can therefore write the observed signal as the difference between the absorption of the orthogonal linear polarization states separated by the polarizing beam splitter (PBS). Since the terms in $m_{0,0}$ are invariant under rotation [24] and cancel in subtraction, the observed differential signal $f(t)$ is proportional to

$$f(t) = m'_{2,0}(t) - m''_{2,0}(t), \quad (2)$$

where m' and m'' denote multipole moments describing the atomic-polarization alignment in the two orthogonal analyzer frames. Rotation of these moments into the laboratory frame yields

$$f(t) = \sqrt{\frac{3}{2}} [m_{2,-1}(t) - m_{2,1}(t)]. \quad (3)$$

The dynamic evolution of multipole moments under the static field \vec{B}_0 and the perturbing field \vec{B}_{rf} can be derived from the Liouville equation [25]. Steady-state oscillating solutions can be found by setting $\dot{m}_{k,q} = 0$ in a frame co-rotating with the perturbing field \vec{B}_{rf} [the rotating wave (RW) frame, denoted $m_{k,q}^{\text{RW}}$]. If the RW frame is chosen such that $\vec{B}_{\text{rf}}(t=0)$ is in the $-x$ direction, we can follow the method of [23], finding solutions for $m_{2,q}^{\text{RW}}$ using

$$\frac{i}{\Gamma} \dot{m}_{2,q}^{\text{RW}} = M_{qq'} m_{2,q'}^{\text{RW}} + i \bar{m}_{2,q}^{\text{RW}}, \quad (4)$$

where Γ is an isotropic spin relaxation rate, $\bar{m}_{2,q}^{\text{RW}}$ are moments describing equilibrium magnetization in the

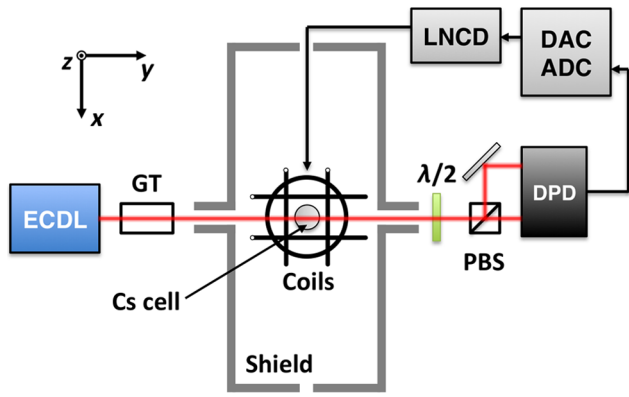


FIG. 2. A schematic of the experimental system, showing the external-cavity diode laser (ECDL), the Glan-Thompson linear polarizer (GT), the magnetometer cell, the five-layer mu-metal shield, the three-axis Helmholtz coils, the half-wave plate ($\lambda/2$), the polarizing beam splitter (PBS), the differential photodetector (DPD), the low-noise coil driver (LNCD), and the data-acquisition system [digital-to-analog converter (DAC) and/or analog-to-digital converter (ADC)]. The coordinate basis is shown in the top left-hand corner and shares the same axes as Fig. 1. The data-acquisition system is controlled using a personal computer (PC) (not shown).

absence of the radio-frequency (rf) field, and

$$M_{qq'} = \begin{pmatrix} 2x - i & S & 0 & 0 & 0 \\ S & x - i & \sqrt{\frac{3}{2}}S & 0 & 0 \\ 0 & \sqrt{\frac{3}{2}}S & -i & \sqrt{\frac{3}{2}}S & 0 \\ 0 & 0 & \sqrt{\frac{3}{2}}S & -x - i & S \\ 0 & 0 & 0 & S & -2x - i \end{pmatrix}. \quad (5)$$

For convenience, we define the dimensionless quantities $x = (\omega_{\text{rf}} - \omega_L)/\Gamma$ and $S = \gamma B_{\text{rf}}^\perp/\Gamma$, where B_{rf}^\perp is the component of \vec{B}_{rf} perpendicular to \vec{B}_0 and γ is the gyromagnetic ratio for the Cs $6^2S_{1/2}$ ($F = 4$) ground state.

We have assumed that optical pumping is weak (the optical-pumping rate is small compared to the spin relaxation rate Γ), ensuring that orientation-alignment conversion [26] is negligible, the atomic-spin relaxation is isotropic, and the equilibrium magnetization $\vec{m}_{k,q}^{\text{RW}}$ is aligned with the static-field vector \vec{B}_0 (i.e., $\vec{m}_{k,q}^{\text{RW}} = \vec{m}$ for $q = 0$, $\vec{m}_{k,q}^{\text{RW}} = 0$ otherwise). The magnitude of \vec{m} is proportional to the projection of $m_{2,0}^{\text{RW}}$ onto $m_{2,0}^{\text{PUMP}}$, where $m_{k,q}^{\text{PUMP}}$ are defined in a frame where the quantization axis is parallel to the polarization axis of the pump light.

Steady-state $\dot{m}_{2,q}^{\text{RW}} = 0$ solutions for $m_{2,q}^{\text{RW}}$ can be found and so $m_{2,q}(t)$ is found by rotation [24]. Substitution into Eq. (3) yields $f(t)$, with terms in $e^{0 \times i\omega_{\text{rf}}t}$, $e^{1 \times i\omega_{\text{rf}}t}$, and $e^{2 \times i\omega_{\text{rf}}t}$. Similarly to [23], we write the amplitude R and phase ϕ of the oscillating responses to \vec{B}_{rf} in the following form:

$$R(\omega_{\text{rf}}) = \frac{A_{1f} [x^2(1 - 2S^2 + 4x^2)^2 + (1 + S^2 + 4x^2)^2]^{1/2}}{(1 + S^2 + x^2)(1 + 4S^2 + 4x^2)}, \quad (6)$$

$$\phi(\omega_{\text{rf}}) = \phi_0^{1f} + \arctan \frac{x(1 - 2S^2 + 4x^2)}{1 + S^2 + 4x^2}, \quad (7)$$

$$R(2\omega_{\text{rf}}) = \frac{A_{2f} [9x^2 + (1 + S^2 - 2x^2)^2]^{1/2}}{(1 + S^2 + x^2)(1 + 4S^2 + 4x^2)}, \quad (8)$$

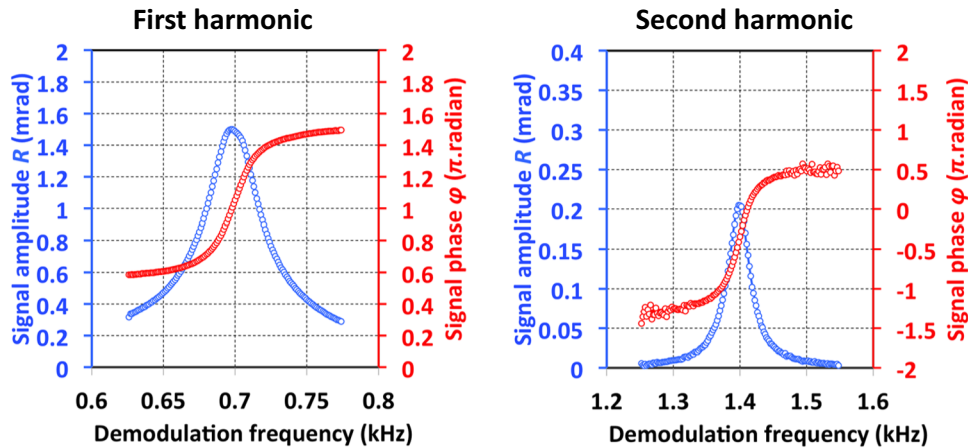


FIG. 3. A measured and fitted magnetic resonance, taken with $|B_0| = 200$ nT applied at $\theta_V = 118^\circ$, $\theta_L = 101^\circ$ and $|B_{\text{rf}}| = 1.5$ nT. A total of 150 segments of data are taken, with a segment sample time of 20 ms. Left: the amplitude (R) and phase (ϕ) components of the first-harmonic demodulated signal. Right: the amplitude (R) and phase (ϕ) of the second-harmonic demodulated signal. The data are fitted with Eqs. (6)–(9), yielding $\omega_L = 2\pi \times 699.60(2)$ Hz, $\Gamma = 12.1(1)$ Hz, $A_{1f} = 107.4(7)$ mV, $\phi_0^{1f} = 0.9672(9)$ π rad, $\phi_0^{2f} = -0.383(6)\pi$ rad, and $\Omega = 2.89(8)$ Hz.

TABLE I. Uncertainties in coil-calibration parameters from the final calibration fit for $|B_0| = 200$ nT. The resulting tolerances in \vec{B}_0 magnitude and orientation are $\delta|B_0| = 54$ pT and $\delta\theta = 0.27$ mrad.

Coil axis	δa (10^{-5})	$\delta\epsilon$ (pT)
x	7.2	11
y	10.0	14
z	9.7	14

$$\phi(2\omega_{\text{rf}}) = \phi_0^{2f} + \arctan \frac{3x}{1 + S^2 - 2x^2}. \quad (9)$$

The on-resonance amplitude A and phase ϕ_0 of the signal vary with θ_L and θ_V as given by the following equations:

$$A_{1f}^2 = \bar{m}^2 S^2 [(\cos \theta_V \cos \theta_L)^2 + (\cos 2\theta_V \sin \theta_L)^2], \quad (10)$$

$$A_{2f}^2 = \bar{m}^2 S^4 \left[\left(\frac{1}{2} \sin 2\theta_V \sin \theta_L \right)^2 + (\sin \theta_V \cos \theta_L)^2 \right], \quad (11)$$

$$\tan \phi_0^{1f} = \frac{-\bar{m}S \cos \theta_V \cos \theta_L}{\bar{m}S \cos 2\theta_V \sin \theta_L}, \quad (12)$$

$$\tan \phi_0^{2f} = \frac{2\bar{m} \sin \theta_V \cos \theta_L}{-\bar{m} \sin 2\theta_V \sin \theta_L}. \quad (13)$$

III. THE TEST SYSTEM

In order to obtain accurate data on the relation of the double-resonance signal phase to the \vec{B}_0 orientation, a shielded test system is used, reducing the effect of background magnetic-field noise and allowing fine control of the \vec{B}_0 orientation. The use of magnetic shielding also allows us to operate in a low-field regime ($|B_0| \approx 200$ nT), in which nonlinear Zeeman splitting, which leads to systematic shifts in the observed magnetic resonance, is negligible compared to the natural linewidth of the magnetic resonance.

Figure 2 shows the test system used and a detailed hardware description can also be found in Ref. [27]. A spherical room-temperature cell of 28 mm diameter containing ^{133}Cs [28] is contained within a five-layer mu-metal shield. The cell contains no buffer gas, but the walls are paraffin coated, extending the atomic-spin lifetime to approximately 100 ms. Optical access is via a 10-mm-diameter axial port and the local static magnetic field at the cell \vec{B}_0 is controlled using three pairs of Helmholtz coils driven by six independent software-controlled current supplies. A Helmholtz coil pair on the z axis is used to apply the

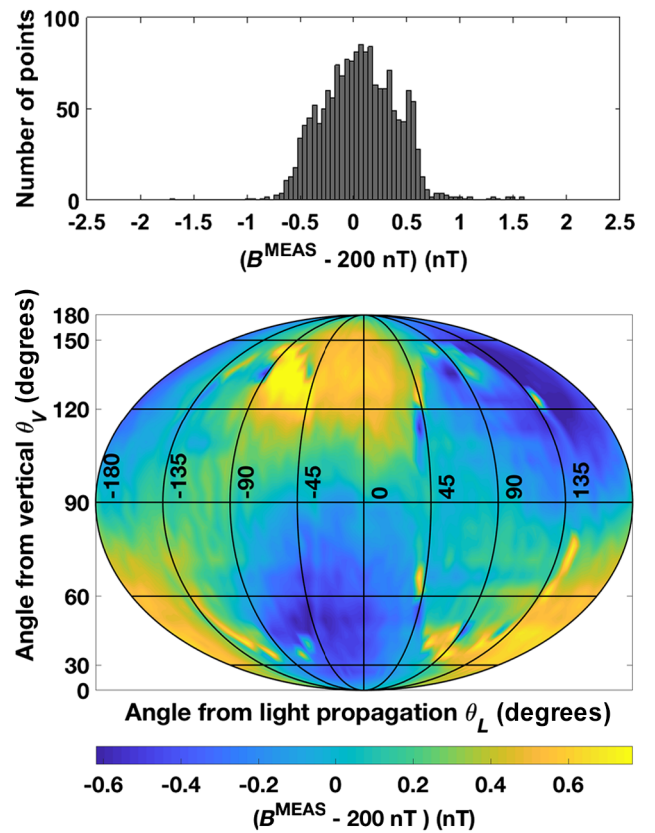


FIG. 4. The measured magnitude of \vec{B}_0 , determined from measurements of ω_L at 1646 different \vec{B}_0 orientations, evenly covering the full solid angle. Top: the distribution of measured $|B_0|$ around the desired field magnitude of 200 nT. The root-mean-square (rms) spread of $|B_0|$ is 302 pT. Bottom: the angular distribution of $|B_0|$.

oscillating perturbation field \vec{B}_{rf} . A 1.4 MHz 16-bit DAC-ADC (National Instruments PCIe-6353) is used to generate \vec{B}_{rf} and digitize the differential photodetector signal. Demodulation is carried out in software.

An external-cavity diode laser (New Focus Vortex 6800) provides optical pump-probe light resonant with the $6^2S_{1/2}$ ($F = 4$) to $6^2P_{1/2}$ ($F = 3$) transition of an external ^{133}Cs reference cell. This beam has a total power of 10 μW , a diameter of 1.2 mm, and is linearly polarized along the x axis prior to the magnetometry cell using a Glan-Thompson polarizer. We note that the modest optical-power requirement would make it possible to replace this commercial laser system with a compact integrated-cavity laser in practical applications.

A single magnetic-resonance measurement is conducted as follows: after the establishment of the desired \vec{B}_0 using the calibrated coil system, an rf modulation signal is generated using the digital-analog converter. The rf modulation frequency ω_{rf} is chirped in finite steps. The detector signal response to the modulation signal is synchronously digitized and a sample segment from each ω_{rf}

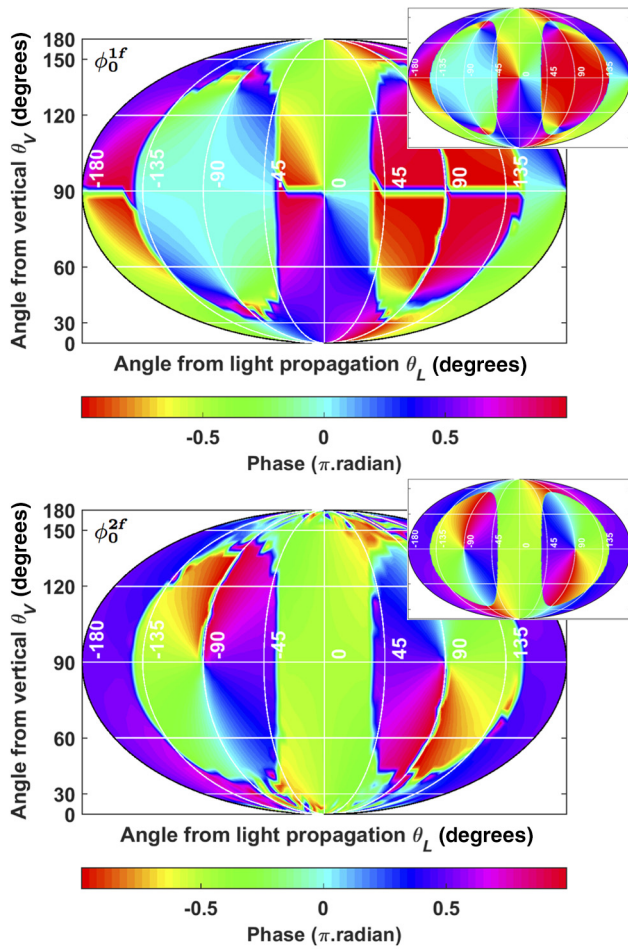


FIG. 5. The observed and (inset) calculated distributions of the on-resonance signal phase with variation of the \vec{B}_0 orientation over the full solid angle. Top: the first-harmonic phase ϕ_0^{1f} . Bottom: the second-harmonic phase ϕ_0^{2f} . The calculated distributions are found using Eqs. (12) and (13).

step demodulated to obtain the in-phase $X(\omega_{rf})$, $X(2\omega_{rf})$ and quadrature $Y(\omega_{rf})$, $Y(2\omega_{rf})$ responses. The sample segments are timed such that each commences in phase with \vec{B}_{rf} and contains an integer number of \vec{B}_{rf} periods. The sample segment length is kept approximately constant for all ω_{rf} , and each sample segment is preceded by a pretrigger segment of fixed duration, to allow the steady-state oscillating response to $\vec{B}_{rf}(\omega_{rf})$ to be measured.

Figure 3 shows the measured signal amplitude $R \equiv \sqrt{X^2 + Y^2}$ and phase $\phi \equiv \arctan(X/Y)$ for data demodulated at ω_{rf} and $2\omega_{rf}$. Least-squares fits of Eqs. (6)–(9) to the data are used to estimate the Larmor frequency ω_L , the spin relaxation rate Γ , the on-resonance signal amplitude A and phase ϕ_0 , and the magnetic Rabi rate Ω .

IV. STATIC-FIELD CALIBRATION

To achieve precise control of \vec{B}_0 , allowing the measurement of orientational effects, the static-field

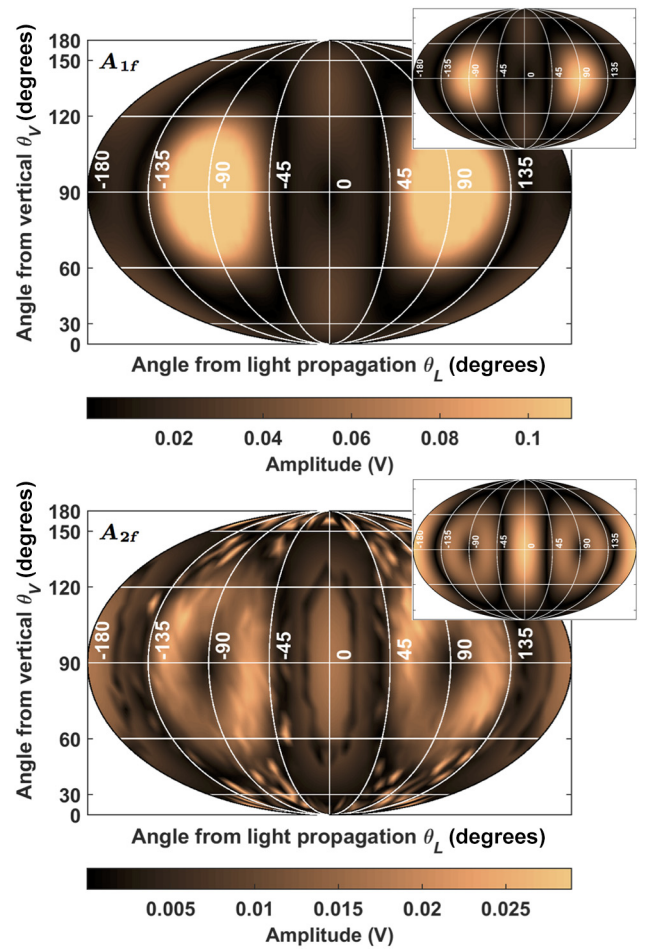


FIG. 6. The observed and (inset) calculated distributions of the on-resonance signal amplitude with variation of the \vec{B}_0 orientation over the full solid angle. Top: the first-harmonic amplitude A_{1f} . Bottom: the second-harmonic amplitude A_{2f} . The polarimeter response to optical rotation is 55.6 V/rad for small rotations. The calculated distributions are found using Eqs. (10) and (11).

generating coils are calibrated by measurement of the Larmor frequency under varying orientations of the applied field. The method for initial coil calibration is described in Ref. [27]. For a given application of the applied field \vec{B}^{APP} , the magnitude of the measured field $|B^{MEAS}| = \omega_L/\gamma$ is determined by fitting Eqs. (6)–(9) to the demodulated data $R(\omega_{rf})$ and $\phi(\omega_{rf})$.

Following the initial calibration, fine coil calibration is carried out by orienting \vec{B}^{APP} in 1646 orientations, spaced with equal angular coverage over the full solid angle, and performing a weighted fit to the observed distribution of $|B^{MEAS}|$ with

$$|B^{MEAS}| = \sqrt{\sum_i (\epsilon_i + a_i B_i^{APP})^2}, \quad (14)$$

where ϵ is the background field and a is a dimensionless coil-calibration factor. The calibration and offset of each

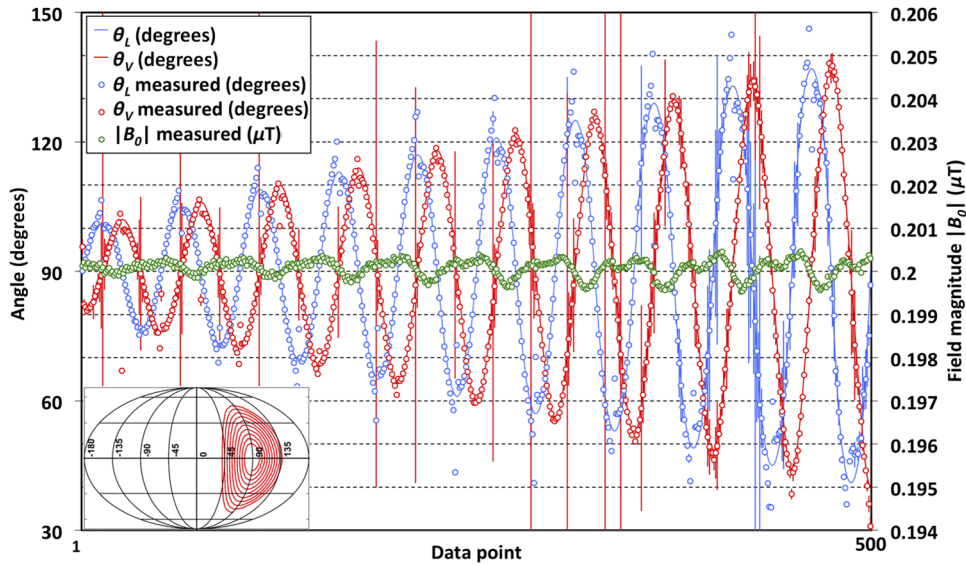


FIG. 7. The measured and set magnetic-field magnitude and orientation for a wide range of \vec{B}_0 orientations. Observed values and uncertainties for θ_V and θ_L are calculated from ϕ_0^{1f} and ϕ_0^{2f} using Eqs. (15) and (16). Uncertainties in $|B_0|$, θ_V , and θ_L are displayed as error bars, which in the case of $|B_0|$ are smaller than the marker. The point of best angular resolution is measured at ($|B_0| = 199.8445(17)$ nT, $\theta_V = 100.986(27)^\circ$, $\theta_L = 118.198(24)^\circ$). The inset in the lower-left corner shows the contour described by successive \vec{B}^{APP} orientations, plotted using the same projection as in Figs. 5 and 6.

coil can then be corrected by the best-fit parameters a_i and ϵ_i . The uncertainties in the fit δa and $\delta \epsilon$ can be used to estimate the tolerances in the magnitude and orientation of \vec{B}_0 , δB_0 , and $\delta \theta$, by assuming that the total field uncertainty, estimated by $\delta B_0 = |\delta \epsilon| + |B_0| |\delta a|$, is perpendicular to \vec{B}_0 , yielding $\delta \theta \approx \delta B_0 / |B_0|$ for $\delta B_0 \ll |B_0|$.

Table I gives the calibration-parameter uncertainties for the final coil calibration and Fig. 4 shows the measured value of $|B_0|$ over the full solid angle for the subsequent field-vector measurements. From the calibration uncertainties, we estimate tolerances of $\delta |B_0| = 54$ pT and $\delta \theta = 0.27$ mrad. The root-mean-square (rms) spread of observed magnitudes $\delta |B_0|^{\text{rms}}$ from Fig. 4 is 302 pT. Although the difference between $\delta |B_0|$ and $\delta |B_0|^{\text{rms}}$ is indicative of some remaining non-normal (i.e., anisotropic and/or systematic) contributions to \vec{B}_0 discrepancies, which result from uncompensated second-order field inhomogeneity and can be seen in the dipolar distribution of residuals in Fig. 4, we can still be confident that the orientation of \vec{B}_0 can be set with fidelity in the milliradian range.

V. VECTOR-FIELD MEASUREMENTS

Equations (10)–(13) indicate a strong dependency between the on-resonance signal components and the orientation of \vec{B}_0 . Using the calibrated field control described above, automated scans of \vec{B}_0 are carried out. Each scan consists of 1646 orientations of \vec{B}_0 , spread over the full solid angle with an approximately even angular distribution. At each \vec{B}_0 orientation, a magnetic-resonance

measurement is carried out, and a fit to the resulting data using Eqs. (6)–(9) is used to obtain best-fit values and uncertainties for ϕ_0^{1f} , ϕ_0^{2f} , A_{1f} , and A_{2f} . The results of this measurement are shown in Figs. 5 and 6. Good agreement is found between the on-resonance signal components in the measured data and Eqs. (10)–(13).

We note the dependence of the first- and second-harmonic on-resonance signal phases ϕ_0^{1f} and ϕ_0^{2f} on the orientation of \vec{B}_0 . From Eqs. (12) and (13), we can derive the following equations for θ_V and θ_L :

$$\tan^2 \theta_V = 1 - \frac{\tan \phi_0^{2f}}{\tan \phi_0^{1f}}, \quad (15)$$

$$\tan \theta_L = \frac{-\cos \theta_V}{\cos 2\theta_V \tan \phi_0^{1f}}. \quad (16)$$

Using Eqs. (15) and (16), the on-resonance phase of first- and second-harmonic signal responses to the rf field can be used to calculate θ_V and θ_L and, along with the fitted Larmor frequency, make a full-vector measurement of \vec{B}_0 .

Figure 7 shows calculated θ_V and θ_L for a range of \vec{B}_0 orientations defined using the calibrated Helmholtz coil system. The range of orientations is shown as an inset to Fig. 7 and is chosen to scan over the zone of high signal amplitude around the light-polarization (x) axis. At each point, the first- and second-harmonic resonance responses are measured for a range of ω_{rf} and fitted using

Eqs. (6)–(9). The on-resonance phases ϕ_0^{1f} and ϕ_0^{2f} are free parameters in this model, and the fit uncertainties are propagated through Eqs. (15) and (16) to give the uncertainties in θ_V and θ_L . The point of highest observed angular resolution has uncertainties of $\delta|B_0| = 1.7$ pT, $\delta\theta_V = 0.027^\circ$, $\delta\theta_L = 0.024^\circ$, giving an overall angular resolution at this point of $\delta\theta = 0.036^\circ$ (0.63 mrad).

VI. CONCLUSIONS

The measurement of complementary field orientation information using a hitherto-scalar double-resonance magnetometry technique has clear potential for impact in practical measurements of arbitrarily oriented fields. Existing three-axis magnetometer data are often transformed to derive data on field magnitude, declination, and inclination. In this work, we demonstrate a scheme for independent measurement of the field vector in this spherical polar basis, while also exploiting the precise and accurate measurement of field magnitude possible with the double-resonance technique. The demonstrated system, with its single-beam thermal-atomic vapor and rf modulation, is an imminently suitable model for scalable portable devices.

The data shown in Fig. 7 demonstrate resolution of the magnetic-field magnitude at the picotesla level and the magnetic-field orientation at the submilliradian level. The variation of the measured field magnitude and orientation from the expected field magnitude (200 nT) and orientation (solid lines) exposes residual calibration errors and uncorrected field inhomogeneity in the Helmholtz coil system, which we establish can set \vec{B}_0 with tolerances in the 100-pT and few-milliradian ranges (Fig. 4). The general validity of the phase-orientation effects derived from theory and observed in Fig. 5 is not called into question but a more stringent test of the absolute accuracy of the field orientation measurement will require improvements to the hardware of the Helmholtz coil system, including improved design tolerances on the coil geometry (currently at the 100- μ m level), improved linearity of the coil current drivers and associated DACs, and addition of higher-order field-gradient compensation coils. These additions would also improve the resolution of the vector-field data.

The double-resonance scheme presented also has some drawbacks in the implementation of practical sensors, which may form the context for further work. We observe dead zones both where the signal amplitude falls to zero (dark regions in Fig. 6) and angular dead zones; orientations for which the observed signal phase has no variation with field orientation $\partial\phi_0/\partial\theta = 0$. These angular dead zones do not necessarily coincide with the signal-amplitude dead zones, and can be seen in Fig. 7 as angular data points with very high uncertainties. A further drawback of this technique is the requirement that magnetic

detuning x be measured independently from phases on resonance ϕ_0^{1f} and ϕ_0^{2f} . In this work, we meet this requirement at the expense of bandwidth by measuring and fitting a ω_{rf} frequency sweep at each data point, demonstrating good field resolution rather than overall sensitivity.

To conclude, we demonstrate an analysis technique for double-resonance alignment magnetometry that can be used to implement vector magnetometry using a scalar device. No additional lasers, field-generating coils, or moving parts are required, and the vector-field sensitivity achieved using this technique could be further enhanced by rapid independent measurement of x , ϕ_0^{1f} , and ϕ_0^{2f} , allowing the field vector $\vec{B}_0(t)$ to be determined with high bandwidth.

ACKNOWLEDGMENTS

The authors would like to thank Professor Antoine Weis and Dr. Victor Lebedev of Fribourg University for supplying the Cs vapor cell used in this work. This work was funded by the UK Quantum Technology Hub in Sensing and Metrology, EPSRC (Grant No. EP/M013294/1). The data shown in this paper are available for download at <http://dx.doi.org/10.15129/5f63ce2-e674-4e42-b923-7550e28d860f>.

-
- [1] M. N. Nabighian, V. J. S. Grauch, R. O. Hansen, T. R. LaFehr, Y. Li, J. W. Peirce, J. D. Phillips, and M. E. Ruder, 75th anniversary: The historical development of the magnetic method in exploration, *Geophysics* **70**, 33ND (2005).
 - [2] Erez Ben-Yosef, Michael Millman, Ron Shaar, Lisa Tauxe, and Oded Lipschits, Six centuries of geomagnetic intensity variations recorded by royal Judean stamped jar handles, *Proc. Natl Acad. Sci.* **114**, 2160 (2017).
 - [3] D. Sheng, A. R. Perry, S. P. Krzyzewski, S. Geller, J. Kitching, and S. Knappe, A microfabricated optically-pumped magnetic gradiometer, *Appl. Phys. Lett.* **110**, 031106 (2017).
 - [4] G. Bevilacqua, V. Biancalana, P. Chessa, and Y. Dancheva, Multichannel optical atomic magnetometer operating in unshielded environment, *Appl. Phys. B: Lasers Opt.* **122**, 103 (2016).
 - [5] S. Pustelny, W. Gawlik, S. M. Rochester, D. F Jackson Kimball, V. V. Yashchuk, and D. Budker, Nonlinear magneto-optical rotation with modulated light in tilted magnetic fields, *Phys. Rev. A* **74**, 063420 (2006).
 - [6] E. Breschi, Z. D. Grujić, P. Knowles, and A. Weis, A high-sensitivity push-pull magnetometer, *Appl. Phys. Lett.* **104**, 023501 (2014).
 - [7] Ricardo Jiménez-Martínez, W. Clark Griffith, Ying Ju Wang, Svenja Knappe, John Kitching, Ken Smith, and Mark D. Prouty, Sensitivity comparison of Mx and frequency-modulated bell-bloom Cs magnetometers in a microfabricated cell, *IEEE Trans. Instrum. Meas.* **59**, 372 (2010).

- [8] T. Zigdon, A. D. Wilson-Gordon, S. Guttikonda, E. J. Bahr, O. Neitzke, S. M. Rochester, and D. Budker, Nonlinear magneto-optical rotation in the presence of a radio-frequency field, *Opt. Express* **18**, 25494 (2010).
- [9] William E. Bell and Arnold L. Bloom, Optically Driven Spin Precession, *Phys. Rev. Lett.* **6**, 280 (1961).
- [10] Arnold L. Bloom, Principles of operation of the rubidium vapor magnetometer, *Appl. Opt.* **1**, 61 (1962).
- [11] Dmitry Budker and Michael Romalis, Optical magnetometry, *Nat. Phys.* **3**, 227 (2007).
- [12] A. Ben-Kish and M. V. Romalis, Dead-Zone-Free Atomic Magnetometry with Simultaneous Excitation of Orientation and Alignment Resonances, *Phys. Rev. Lett.* **105**, 193601 (2010).
- [13] Swarupananda Pradhan, Three axis vector atomic magnetometer utilizing polarimetric technique, *Rev. Sci. Instrum.* **87**, 093105 (2016).
- [14] S. J. Seltzer and M. V. Romalis, Unshielded three-axis vector operation of a spin-exchange-relaxation-free atomic magnetometer, *Appl. Phys. Lett.* **85**, 4804 (2004).
- [15] S. Afach, G. Ban, G. Bison, K. Bodek, Z. Chowdhuri, Z. D. Grujić, L. Hayen, V. H elaine, M. Kasprzak, K. Kirch, P. Knowles, H.-C. Koch, S. Komposch, A. Kozela, J. Kempel, B. Lauss, T. Lefort, Y. Lemi ere, A. Mtchedlishvili, O. Naviliat-Cuncic, F. M. Piegsa, P. N. Prashanth, G. Qu em ener, M. Rawlik, D. Ries, S. Roccia, D. Rozpedzik, P. Schmidt-Wellenburg, N. Severjins, A. Weis, E. Wursten, G. Wyszynski, J. Zejma, and G. Zsigmond, Highly stable atomic vector magnetometer based on free spin precession, *Opt. Express* **23**, 22108 (2015).
- [16] Wei-Min Sun, Quiang Huang, Zong-Jun Huang, Ping-Wen Wang, and Jun-Hai Zhang, All-optical vector cesium magnetometer, *Chin. Phys. Lett.* **34**, 058501 (2017).
- [17] B. Patton, E. Zhivun, D. C. Hovde, and D. Budker, All-Optical Vector Atomic Magnetometer, *Phys. Rev. Lett.* **113**, 013001 (2014).
- [18] Kevin Cox, Valery I. Yudin, Alexey V. Taichenachev, Irina Novikova, and Eugeniy E. Mikhailov, Measurements of the magnetic field vector using multiple electromagnetically induced transparency resonances in Rb vapor, *Phys. Rev. A* **83**, 015801 (2011).
- [19] A. J. Fairweather and M. J. Usher, A vector rubidium magnetometer, *J. Phys. E: Sci. Instrum.* **5**, 986 (1972).
- [20] L. Lenci, A. Auyuanet, S. Barreiro, P. Valente, A. Lezama, and H. Failache, Vectorial atomic magnetometer based on coherent transients of laser absorption in Rb vapor, *Phys. Rev. A* **89**, 043836 (2014).
- [21] A. K. Vershovskii, M. V. Balabas, A.  . Ivanov, V. N. Kulyasov, A. S. Pazgalev, and E. B. Aleksandrov, Fast three-component magnetometer-variometer based on a cesium sensor, *Tech. Phys.* **51**, 112 (2006).
- [22] Marcis Auzinsh, Dmitry Budker, and Simon Rochester, *Optically Polarized Atoms* (Oxford University Press, Oxford, 2010).
- [23] Antoine Weis, Georg Bison, and Anatoly S. Pazgalev, Theory of double resonance magnetometers based on atomic alignment, *Phys. Rev. A* **74**, 033401 (2006).
- [24] M. A. Morrison and G. A. Parker, A guide to rotations in quantum mechanics, *Aust. J. Phys.* **40**, 465 (1987).
- [25] Stuart J. Ingleby, Carolyn O'Dwyer, Paul F. Griffin, Aidan S. Arnold, and Erling Riis, Orientational effects on the amplitude and phase of polarimeter signals in double-resonance atomic magnetometry, *Phys. Rev. A* **96**, 013429 (2017).
- [26] S. M. Rochester, M. P. Ledbetter, T. Zigdon, A. D. Wilson-Gordon, and D. Budker, Orientation-to-alignment conversion and spin squeezing, *Phys. Rev. A* **85**, 022125 (2012).
- [27] S. J. Ingleby, P. F. Griffin, A. S. Arnold, M. Chouliara, and E. Riis, High-precision control of static magnetic field magnitude, orientation, and gradient using optically pumped vapour cell magnetometry, *Rev. Sci. Instrum.* **88**, 043109 (2017).
- [28] N. Castagna, G. Bison, G. Di Domenico, A. Hofer, P. Knowles, C. Macchione, H. Saudan, and A. Weis, A large sample study of spin relaxation and magnetometric sensitivity of paraffin-coated Cs vapor cells, *Appl. Phys. B* **96**, 763 (2009).